Available online at www.sciencedirect.com
SCIENCE DIRECT®
Catalysis Today 85 (2003) 177–192
CATALYSIS TODAY
www.elsevier.com/locate/cattod

Electronic and chemical properties of mixed-metal oxides: basic principles for the design of $DeNO_x$ and $DeSO_x$ catalysts

José A. Rodriguez*

Chemistry Department, Brookhaven National Laboratory, Upton, NY 11973, USA

Received 15 January 2003; received in revised form 26 March 2003; accepted 28 March 2003

Abstract

Correlations between the electronic and chemical properties of perovskites, molybdates, and metal-doped MgO or CeO_2 are examined. Simple models based on band-orbital mixing can explain trends found for the interaction of these catalytic materials with adsorbates: the less stable the occupied levels of a mixed-metal oxide, the higher its chemical reactivity. Metal ↔ oxygen ↔ metal interactions are common in mixed-metal oxides and can lead to substantial changes in the electronic and chemical properties of the cations. This is particularly true in the case of ABO_3 perovskites (A = Pb, Ca, Sr, Li, K, Na; B = Ti, Zr, Nb), and it is an important phenomenon that has to be considered when mixing AO and BO_2 oxides for catalytic applications. In systems like $Ce_{1-x}Zr_xO_2$ and $Ce_{1-x}Ca_xO_2$, the structural stress induced by the dopant (Zr or Ca) leads to perturbations in the electronic properties of the Ce cations. The trends in the behavior of metal-doped MgO illustrate a basic principle in the design of mixed-metal oxide catalysts for $DeNO_x$ and $DeSO_x$ operations. The general idea is to find metal dopants that upon hybridization within an oxide matrix remain in a relatively low oxidation state and at the same time induce occupied electronic states located well above the valence band of the host oxide. Electronic effects should not be neglected a priori when explaining the behavior or dealing with the design of mixed-metal oxide catalysts.

Keywords: Mixed-metal oxides; Electronic effects; $DeNO_x$ and $DeSO_x$

1. Introduction

Mixed-metal oxides play a very important role in many areas of chemistry, physics, materials science, and geochemistry [1–6]. In technological applications, they are used in the fabrication of microelectronic circuits, piezoelectric devices and as catalysts [3–7]. Over the years there has been a strong interest in understanding the behavior of mixed-metal oxide catalysts [4,5,7–9]. Mixed-metal oxides are active catalysts for the selective hydrogenation and isomerization of olefins, the water-gas shift reaction, dehydrogenation of alcohols, the oxidation of CO and alkanes, NO reduction, SO_2 destruction, photolysis of water, etc. [5,7,8]. In principle, several phenomena can contribute to the superior performance of these complex systems [4,5,7], and scientific criteria are badly needed for choosing the "right" combination of elements when designing a mixed-metal oxide catalyst [4,8,9].

For example, $PbTiO_3$ and $PbZr_xTi_{1-x}O_3$ ($x < 0.6$) are able to catalyze the reduction of SO_2 ($SO_2 + 2H_2S \rightarrow 2H_2O + 3S_{solid}$; $SO_2 + 2CO \rightarrow 2CO_2 + S_{solid}$) or the oxidation of CO and hydrocarbons at least 7–12 times faster than the individual oxides (TiO_2, ZrO_2, PbO) [7,10]. The phenomena

* Tel.: +1-631-344-2246; fax: +1-631-344-5815.
E-mail address: rodrigez@bnl.gov (J.A. Rodriguez).

0920-5861/$ – see front matter © 2003 Elsevier B.V. All rights reserved.
doi:10.1016/S0920-5861(03)00385-7

behind this remarkable trend are not well understood and there is a general desire to replace lead (a health hazard and environmental contaminant) in the crystal structures of $PbTiO_3$ and $PbZr_xTi_{1-x}O_3$ [7,10,11]. Another interesting case of study is metal-doped MgO [4,8,12]. Metal-doped MgO is used as a catalysts for the oxidative coupling of methane to produce C_2 hydrocarbons [8,13], the reforming of CH_4 with CO_2 or H_2O [8,14], and reactions associated with the control of atmospheric pollution [7,15,16]. Big variations in catalytic activity have been observed when changing the second metal or dopant agent [7,8,13–15]. The causes for these changes in activity are not well understood and more basic knowledge is necessary for improving the performance of metal-doped MgO catalysts [7,8,13]. Due to its redox properties, CeO_2 is a key component in catalysts commonly used to reduce the emissions of CO, NO_x and hydrocarbons from automobile exhaust [17]. To enhance the redox properties and thermal stability of pure ceria, zirconia is often mixed as an additive to form solid solutions of the $Ce_{1-x}Zr_xO_2$ type [17,18]. The mechanisms for the doping effects of Zr remain uncertain and are still a matter of debate [17–19].

With respect to single-metal oxides, the chemical behavior of mixed-metal oxides may be different as a consequence of several factors. In some situations, the cations in a mixed-metal oxide can work in a cooperative way catalyzing different steps of a chemical process. Furthermore, the combination of two metals in an oxide matrix can produce materials with novel structural or electronic properties that can lead to superior catalytic activity or selectivity. At a structural level, a dopant can introduce stress into the lattice of an oxide host, inducing in this way the formation of defects that have a high chemical activity. On the other hand, the lattice of the oxide host can impose on the dopant element non-typical coordination modes with a subsequent perturbation in the dopant chemical properties. Finally, metal ↔ metal or metal ↔ oxygen ↔ metal interactions in mixed-metal oxides can give electronic states not seen in single-metal oxides. In recent studies [9,11,12,15,16,20,21] we have found a direct link between the electronic and chemical properties of a large series of mixed-metal oxides. It is worthwhile to explore the general validity of such correlation since it can be useful as a basic criterium for the design of mixed-metal oxide catalysts.

In this short review article, we examine the behavior of four different kinds of mixed-metal oxides. First, we deal with the properties of perovskites of the ABO_3 type (A = Pb, Ca, Sr, Li, K, Na; B = Ti, Zr, Nb). Then, works for $XMoO_4$ molybdates (X = Fe, Co, Ni, Mg) are presented. This is followed by systematic studies on metal-doped magnesium oxide ($TM_xMg_{1-x}O$, TM = Cr, Mn, Fe, Co, Ni, Sn, Zn). At the end, we discuss on-going investigations for $Ce_{1-x}Zr_xO_2$ and $Ce_{1-x}Ca_xO_2$ systems.

2. Electronic and chemical properties of ABO_3 perovskites

Perovskites with an ABO_3 stoichiometry (where A is a mono- or divalent cation, and B a penta- or tetra-valent transition metal atom) are among the most important ferroelectric materials [3] and active catalysts for many reactions [5,7]. Fig. 1 shows the cubic structure usually adopted by ABO_3 perovskites [3,5]. Each A cation is in an octahedral coordination surrounded by six O atoms, whereas each B cation has 12 O neighbors. In some systems a tetragonal distorsion occurs [3].

Table 1 compares calculated charge distributions for typical ABO_3 perovskites and the corresponding BO_2 oxides [11,22]. The listed values are for the ideal cubic structures of the perovskites (Fig. 1). No significant changes in charge distribution were found when going from cubic to tetragonal structures in $PbTiO_3$, $KNbO_3$ or $CaZrO_3$ [11]. Some of these mixed-metal oxide systems have been the subject of extensive research [1,11,22–24], and it is well established that they are far from being fully ionic. The important point here is that

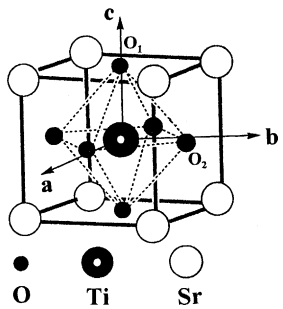

Fig. 1. Cubic unit cell for ABO_3 perovskites, in this case $SrTiO_3$.

Table 1
Calculated charges in ABO_3, AO and BO_2 oxides (electron)[a]

Compound	q(O)	q(B)	q(A)
$PbTiO_3$	−0.75	0.63	1.63
$CaTiO_3$	−0.88	0.69	1.93
$SrTiO_3$	−0.88	0.68	1.96
PbO	−0.92	–	0.92
CaO	−1.66	–	1.66
SrO	−1.65	–	1.65
TiO_2 (rutile)	−0.67	1.34	–
TiO_2 (anatase)	−0.68	1.37	–
$PbZrO_3$	−0.83	0.84	1.65
$CaZrO_3$	−0.95	0.91	1.94
$SrZrO_3$	−0.96	0.90	1.97
ZrO_2 (cubic)	−0.78	1.56	–
ZrO_2 (monoclinic)	−0.78	1.55	–
$LiNbO_3$	−0.74	1.19	1.03
$NaNbO_3$	−0.74	0.91	1.30
$KNbO_3$	−0.83	0.94	1.56
$RbNbO_3$	−0.82	1.16	1.29
$CsNbO_3$	−0.83	1.08	1.42
NbO_2	−0.70	1.40	–

[a] Obtained from DF calculations using the Mulliken approach for charge partition [11].

in all the cases examined there is a large decrease in the positive charge on the B element (Ti, Zr, Nb) when going from a single oxide in a *formal* oxidation state of "+4" (TiO_2, ZrO_2, NbO_2) to perovskite structures in which the formal oxidation state of B is also "+4". Ti is the most affected, and Nb the least. The crystal structures of PbO, CaO and SrO are well known [1]. For the cations in these oxides, we calculated charges of +0.92*e* (Pb), +1.66*e* (Ca) and +1.65*e* (Sr) [11]. These charges are smaller than those found for the A cations in the $PbBO_3$, $CaBO_3$ and $SrBO_3$ systems of Table 1. Thus, it appears that metal ↔ oxygen ↔ metal interactions affect the electron density of both the A and B cations in the perovskite. In this respect, the ABO_3 compounds follow the phenomenological model proposed by Barr et al. [2,25,26]: in the mixing of two oxides (AO and BO_2), the cation of the more ionic oxide is expected to become even more ionic, while the cation of the more covalent oxide should experience a corresponding increase in covalency. This phenomenon opens the possibility of large variations in the chemical properties of the metal atoms and must be taken into consideration when mixing AO and BO_2 oxides for catalytic applications [11,22,27,28].

For the mixed-metal oxides listed in Table 1, the TiO_2-terminated (1 0 0) face of $SrTiO_3$ is the best known and most studied surface [1,22–24,27–31]. Recent works have examined the adsorption of NO [27], H_2O [28,30] and SO_2 [22,28] on this surface. The bottom panel of Fig. 2 shows a N 1s XPS spectrum acquired after dosing NO to a $SrTiO_3$(1 0 0) surface at 100 K [27]. Only a single peak is observed at ∼401 eV. This peak position corresponds to chemisorbed NO. Upon heating from 100 to 300 K, most of the NO signal disappears and no new peak is detected in the N 1s region. The center and top panels in Fig. 2 illustrate the effect of O vacancies (associated with Ti^{3+} and Ti^{2+} sites) on the chemistry of adsorbed NO. On the fully oxidized surface only NO is present, whereas a mixture of NO, N_2O and N_x species is seen on the partially reduced $SrTiO_3$(1 0 0) surface [27]. Oxygen vacancies are also necessary to induce the dissociation of H_2O [28,30] and SO_2 [22,28].

Fig. 3 shows a series of NO-TPD spectra for NO/$SrTiO_3$(1 0 0) as a function of exposure at 100 K [27]. The TPD results indicate that there are at least three different types of adsorption states on the oxide surface. The peak near 125 K can be assigned to desorption of a physisorbed multilayer of NO. The main peak at 260 K probably corresponds to NO bonded to TiO_2 terraces of strontium titanate, and the long tail to NO bonded to defects or imperfections in the oxide surface [27]. The experiments of TPD show that at small coverages, NO desorbs at much higher temperatures from $SrTiO_3$(1 0 0), ∼260 K [27], than from TiO_2(1 1 0), ∼130 K [32]. From these experiments, one can estimate NO adsorption energies of 16 kcal/mol on $SrTiO_3$(1 0 0) and 8 kcal/mol on TiO_2(1 1 0). Density functional (DF) slab calculations predict adsorption energies of 14.1 and 9.4 kcal/mol for NO on Ti sites of perfect $SrTiO_3$(1 0 0) and TiO_2(1 1 0) surfaces [27]. Since, the Ti–O bonds in $SrTiO_3$ are more covalent than in TiO_2, the Ti centers in the mixed-metal oxide can respond better to the presence of an adsorbate that has electron-acceptor properties like NO [33]. SO_2 also has electron-acceptor properties [34] and bonds stronger to $SrTiO_3$(1 0 0) than to TiO_2(1 1 0) (adsorption energies of 14.4 and 10.3 kcal/mol, respectively) [22]. An opposite trend can be expected for the adsorption of molecules that are good electron-donors or have a high basicity. Indeed, TPD spectra show

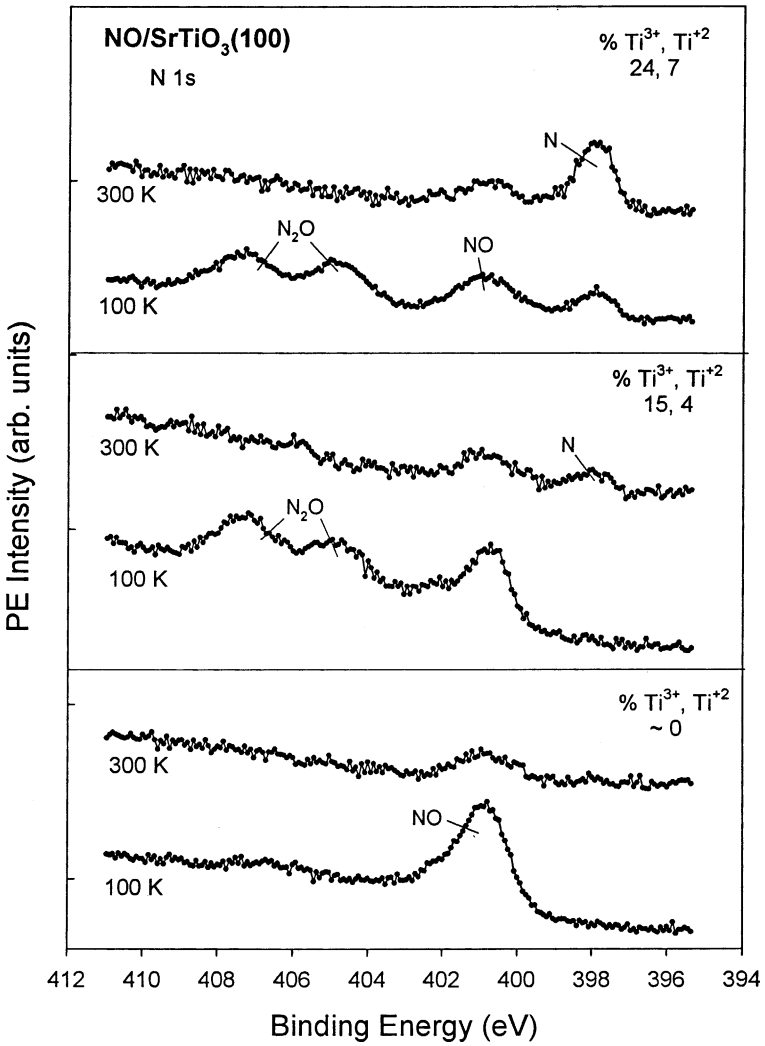

Fig. 2. N 1s XPS spectra for the adsorption of NO on $SrTiO_3$(1 0 0) and $SrTiO_{3-x}$(1 0 0) surfaces at 100 K. The $SrTiO_{3-x}$(1 0 0) substrates were prepared by ion sputtering $SrTiO_3$(1 0 0). For the reduced surface in the center panel, the Ti 2p spectrum contained 15% of Ti^{3+} and 4% of Ti^{2+} before the dosing of NO. The corresponding values for the reduced surface in the top panel are 24% of Ti^{3+} and 7% of Ti^{2+}. After the dosing of 0.5 l of NO at 100 K, each system was heated to 300 K (from Ref. [27]).

that water desorbs at much lower temperatures from the TiO_2-terminated face of $SrTiO_3$(1 0 0) than from a TiO_2(1 1 0) surface [30]. The relatively low positive charge on the Ti cations of $SrTiO_3$(1 0 0) leads to weak bonding interactions with the O lone-pairs of water [28].

When comparing the catalytic activity of $SrTiO_3$ and TiO_2 for the reduction of NO (or SO_2) and other chemical processes [5,7,10], one finds that the mixed-metal oxide is the better catalyst. The strong metal:oxygen:metal interactions that drastically modify the electron density of Ti in $SrTiO_3$ are also present in the other ABO_3 compounds listed in Table 1. These electronic perturbations could eventually affect the chemical properties of the metal cations as seen for the case of $SrTiO_3$. This type of phenomenon must be taken into consideration when dealing with the design of ABO_3 perovskite catalysts [22,27,28]. In general,

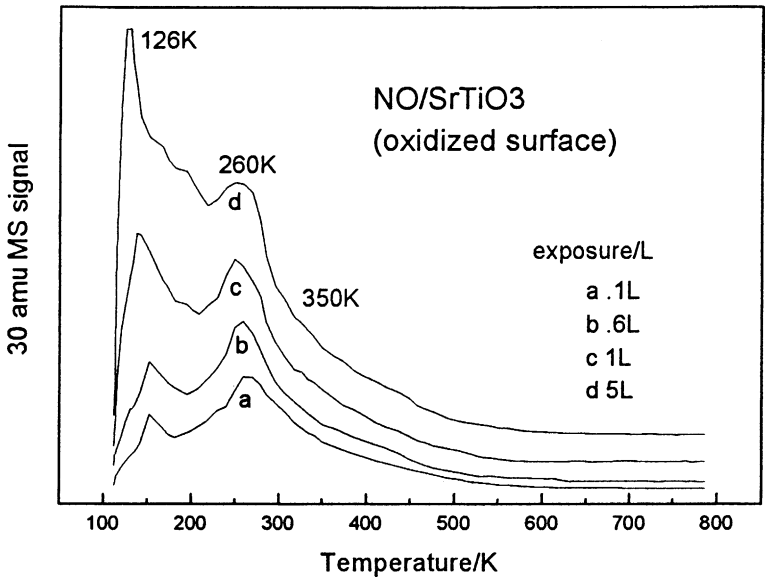

Fig. 3. NO-TPD spectra for NO/$SrTiO_3$(1 0 0) as a function of NO exposure at 100 K. Heating rate ~4.2 K/s (from Ref. [27]).

a simple extrapolation of the catalytic performance of the individual AO and BO_2 oxides is not a reliable assumption.

3. Electronic and chemical properties of molybdates

Molybdenum is able to form stable oxides in combination with many metals [8,35]. Molybdates of the $XMoO_4$ type (X = Mg, Fe, Co, Ni) have been detected in industrial catalysts used for hydrodesulfurization processes or for the partial oxidation of alcohols and hydrocarbons [36,37]. At atmospheric pressure, two phases, usually designed as α and β, are known of $CoMoO_4$ and $NiMoO_4$ (see Fig. 4) [20,35,37]. The main difference between them is in the coordination of the Mo^{6+} ions, pseudo-octahedral in the α-phase and tetrahedral in the β-phase. In both isomorphs, the Co^{2+} and Ni^{2+} ions occupy sites with octahedral coordination. $FeMoO_4$ and $MgMoO_4$ adopt only a β-phase crystal structure under normal conditions [20,21].

Table 2 shows charges obtained in DF calculations for the β-phases of $MgMoO_4$, $FeMoO_4$, $CoMoO_4$ and $NiMoO_4$ [38].[1] In these systems, no big variations were found between the calculated charge distributions in the α- and β-phases [20,38] (see footnote 1). For comparison the calculated cation charges for MoO_3, MgO, FeO, CoO and NiO are also listed in Table 2. In these single-metal oxides the cations are always in an octahedral coordination [29,39]. MgO, FeO, CoO and NiO adopt a rock-salt structure [39]. After taking into consideration the stoichiometry of oxygen in each compound, the calculated charges on the metal cations indicate that the metal–oxygen bonds in MoO_3 are somewhat more covalent than in MgO, FeO, and NiO (1.60*e*/3 versus 1.40*e*, 0.73*e* and 0.68*e*).

Table 2
Calculated charges in $XMoO_4$, MoO_3 and XO oxides (electron)

Compound	*q*(X)	*q*(Mo)
MoO_3	–	1.60
β-$MgMoO_4$	1.72, 1.75[a]	1.43, 1.46[a]
MgO	1.40	–
β-$FeMoO_4$	0.88, 0.91	1.51, 1.52
FeO	0.73	–
β-$CoMoO_4$	0.54, 0.56	1.54, 1.58
CoO	0.54	–
β-$NiMoO_4$	0.78, 0.87	1.56, 1.57
NiO	0.68	–

[a] There are two types of X and Mo atoms within the unit cell of the β-$XMoO_4$ compounds [20,21].

[1] Calculated as in Ref. [11] using a Mulliken population analysis.

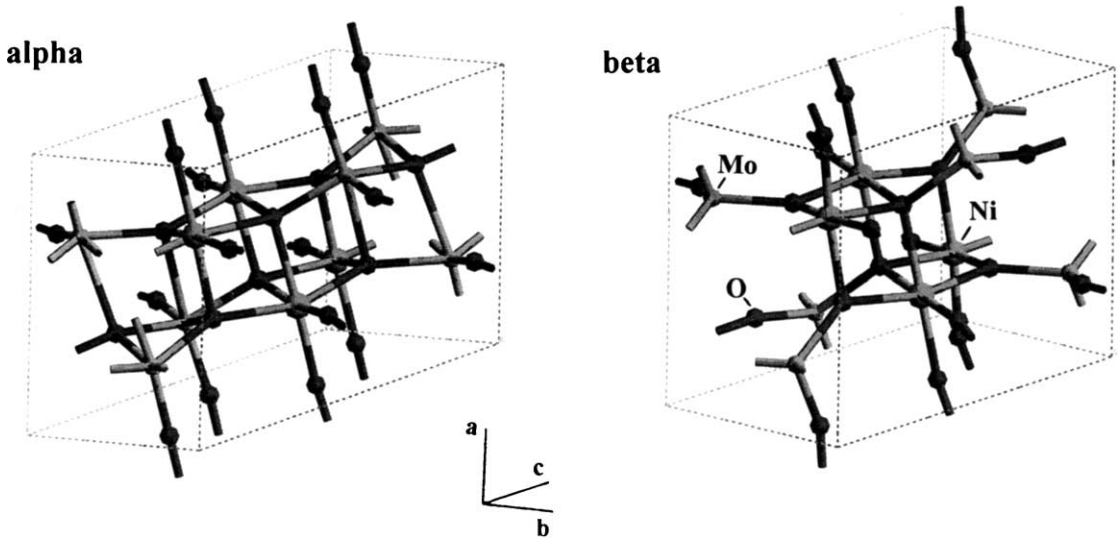

Fig. 4. Primitive cells for the α- (left-side panel) and β-phases (right-side panel) of $XMoO_4$ (X = Mg, Fe, Co or Ni) molybdates. The dark spheres represent O atoms. The metal atoms are represented by the small (Mo) or large gray spheres (Mg, Fe, Co or Ni). As an example, the crystal structures of $NiMoO_4$ are shown in the figure.

The $XMoO_4$ mixed-metal oxides obey the Barr model [2,25,26]: in the mixing of XO and MoO_3 oxides, the cation of the more ionic oxide (XO) becomes even more ionic, while the cation of the more covalent oxide (MoO_3) experiences an increase in covalency. But in the $XMoO_4$ systems the variations in cation charge with respect to the corresponding XO and MoO_3 oxides are not big. β-$MgMoO_4$ exhibits the most substantial perturbations in cation charge (Mg: 1.40e →∼ 1.73e; Mo: 1.60e →∼ 1.44e) and they are not as large as those seen in Table 1 for the cations of ABO_3 perovskites.

The left-hand panel in Fig. 5 shows calculated (DF) density-of-states plots for β-$MgMoO_4$, β-$NiMoO_4$ and β-$FeMoO_4$ [20,21]. Only occupied states (OS) are included in the graph. For β-$MgMoO_4$, the density-of-states plot near the top of the valence band is very similar to that of pure MoO_3 [20]. β-$NiMoO_4$ displays a large density-of-states near the top of the valence band that is not observed for β-$MgMoO_4$ or MoO_3 [20]. In this respect, β-$FeMoO_4$ is an intermediate case between β-$NiMoO_4$ and β-$MgMoO_4$ [21]. Also, the Ni 3d states in β-$NiMoO_4$ are energetically less stable than the Fe 3d states in β-$FeMoO_4$ or the Mg 3s states in β-$MgMoO_4$. These trends suggest that $NiMoO_4$ should be more chemically active than $FeMoO_4$, $MgMoO_4$ or MoO_3 [20,21]. The right-hand panel in Fig. 5 displays results of X-ray absorption near-edge spectroscopy (XANES) collected after dosing the same amount of H_2S to MoO_3 and $XMoO_4$ oxides at 400 °C [21]. The molybdates were only partially sulfided, and the XANES data indicate that their chemical reactivity increases in the sequence: MoO_3 ≈ β-$MgMoO_4$ < β-$FeMoO_4$ < β-$NiMoO_4$. An identical sequence is obtained after analyzing experimental data for the reaction of H_2 with the molybdates [20]. Results of temperature programmed reduction show that the consumption of H_2 starts around 500 °C for β-$NiMoO_4$, 600 °C for β-$MgMoO_4$, and 650 °C for MoO_3 [20,37,40]. For the oxidative dehydrogenation of alkanes, β-$NiMoO_4$ is a much better catalyst than β-$MgMoO_4$ [40,41]. Therefore, one can conclude that there is a correlation between the electronic and chemical properties of the $XMoO_4$ molybdates: the less stable the top of the valence band in the mixed-metal oxide, the higher the chemical reactivity of the system. In the next section, we will show that such correlation is also valid for explaining the chemical behavior of metal-doped MgO, and it can be a useful criterium in the design of mixed-metal oxide catalysts.

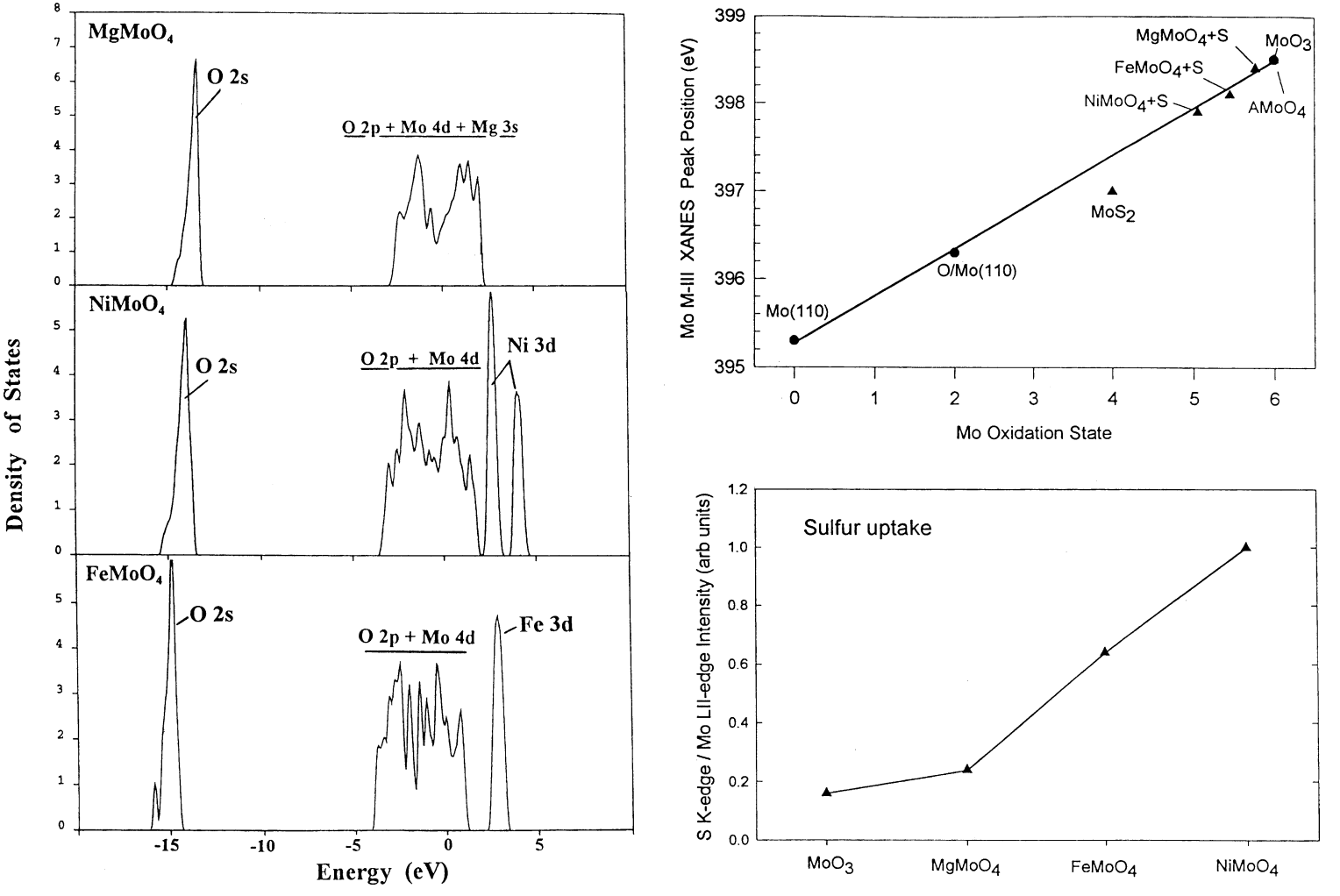

Fig. 5. Left: calculated (DF) density-of-states for the occupied bands of β-$MgMoO_4$, β-$NiMoO_4$, and β-$FeMoO_4$. The "zero" of energy is not the vacuum level. Right: results of XANES for the adsorption of H_2S on MoO_3, β-$MgMoO_4$, β-$NiMoO_4$, and β-$FeMoO_4$ at 400 °C (from Ref. [21]).

4. Electronic and chemical properties of metal-doped MgO

Doping with a transition metal can drastically change the catalytic properties of magnesium oxide, making it very active for the activation of methane and the destruction of NO_x and SO_x species [4,7,8,13–16]. At low concentrations, many transition metals form solid solutions in magnesium oxide ($TM_xMg_{1-x}O$, TM = Cr, Mn, Fe, Co, Ni, Rh, Pd, Pt, etc.) [7,13,14]. In these solid solutions, the second metal (dopant agent) occupies magnesium sites within the typical rock-salt structure of MgO. From a charge balance, a formal oxidation state of "+2" can be expected for the metal dopant if one assumes formal charges of "−2" and "+2" for O and Mg [12,42]. Photoemission experiments and DF calculations show big changes in the electronic properties of $TM_xMg_{1-x}O$ depending on the nature of the dopant agent [12,15,16].

The right-hand panel in Fig. 6 displays valence spectra for a pure MgO(1 0 0) film, and systems containing a small amount of Zn, Ni, Fe and Cr [16]. The valence spectrum for the MgO(1 0 0) film agrees very well with spectra reported in the literature for bulk MgO [29]. In these spectra, the dominant O 2p band has a width of ∼6 eV, and appears at ∼4 eV below the Fermi level (0 of energy). Doping induces the appearance of occupied electronic states *above* the valence band of MgO. The presence of these states is also observed in DF slab calculations for the $TM_xMg_{1-x}O$(1 0 0) systems (left-side of Fig. 6) [12,15,16]. In the case of

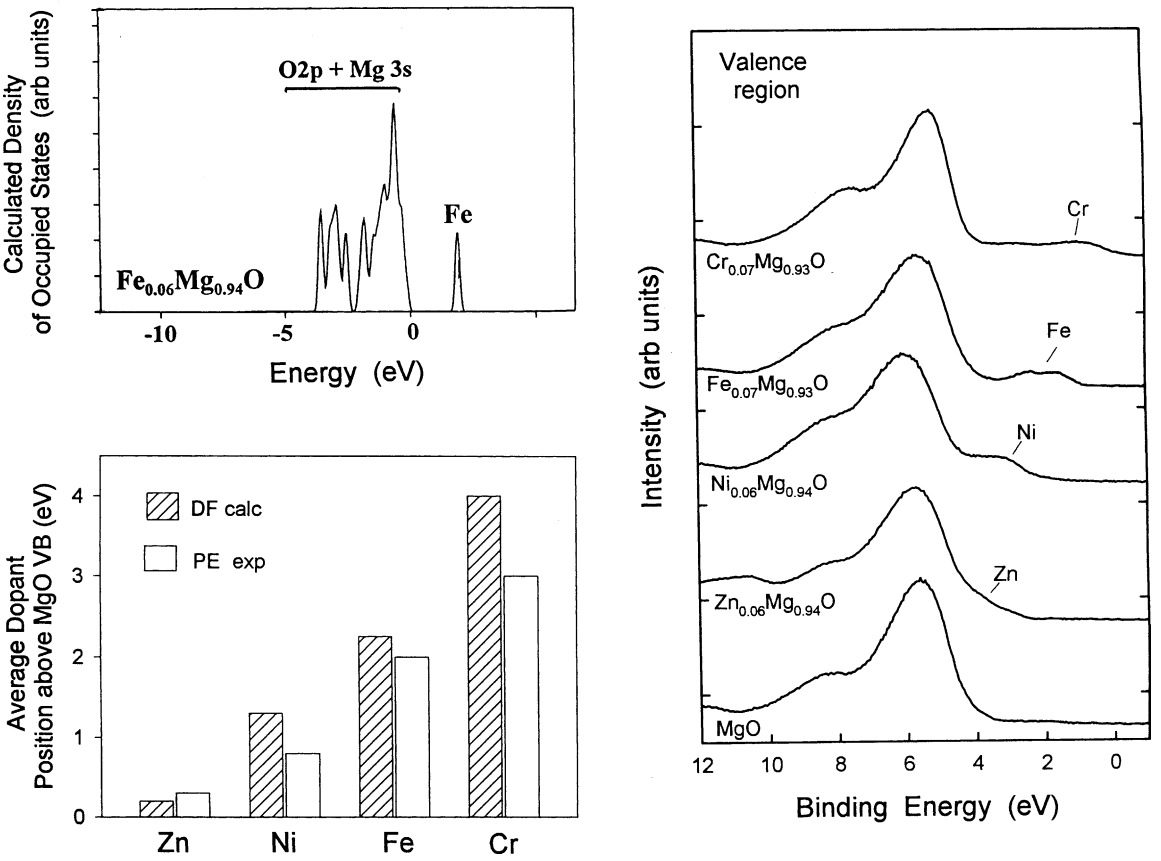

Fig. 6. Left, top: calculated (DF) density-of-states for the occupied bands of a $Fe_{0.06}Mg_{0.94}O$(1 0 0) slab. The zero of energy is not the vacuum level. Left, bottom: average position of the dopant levels in $TM_{0.06}Mg_{0.94}O$(1 0 0). Results of DF calculations and photoemission (PE) experiments. Right: valence UPS spectra for MgO(1 0 0) and a series of $TM_xMg_{1-x}O$(1 0 0) systems (from Ref. [16]).

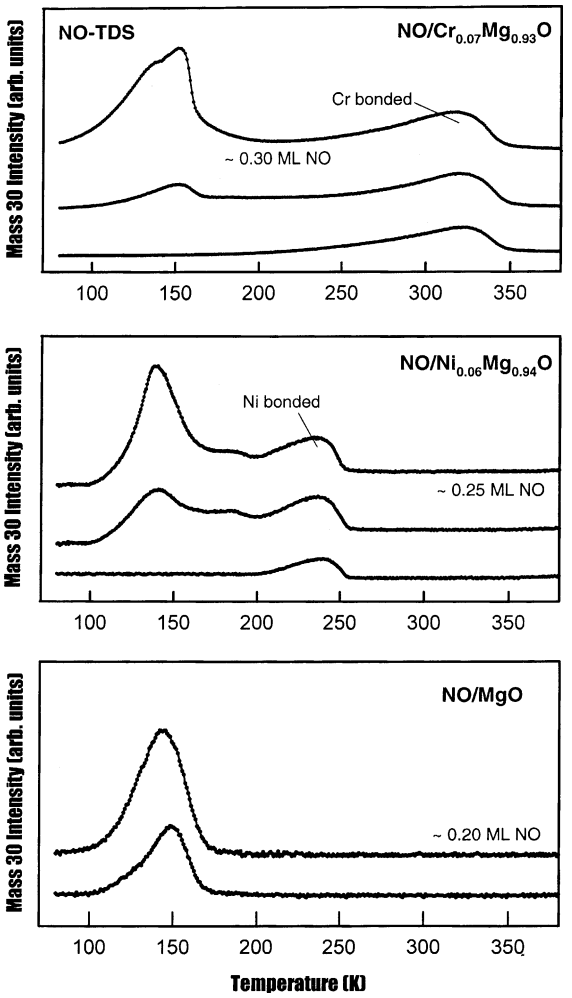

Fig. 7. NO thermal desorption spectra for MgO(1 0 0), $Ni_{0.06}Mg_{0.94}O(1\,0\,0)$, and $Cr_{0.07}Mg_{0.93}O(1\,0\,0)$ films. The NO molecule was dosed at 80 K. In the final step of each experiment, the oxide surface was saturated with NO. Heating rate = 2 K/s (from Ref. [12]).

$Zn_{0.06}Mg_{0.94}O(1\,0\,0)$, the new states almost overlap with the valence band of the host oxide. On the other hand, for $Cr_{0.07}Mg_{0.93}O(1\,0\,0)$, the Cr-induced states are located well above the MgO valence band.

The bottom panel in Fig. 7 shows NO-TPD data acquired after saturating the surface of a MgO(1 0 0) film with NO at 80 K [12]. A small amount of NO (~0.2 ML) is present on imperfections of the MgO(1 0 0) surface and desorbs around 140 K. From a Redhead analysis, one can estimate a NO adsorption energy of ~8 kcal/mol [12]. Fig. 7 also displays TPD data for $NO/Ni_{0.06}Mg_{0.94}O(1\,0\,0)$ and $NO/Cr_{0.07}Mg_{0.93}O(1\,0\,0)$ systems. Photoemission measurements indicate that NO does not dissociate on these surfaces [15]. The NO-TPD spectra for $NO/Ni_{0.06}Mg_{0.94}O(1\,0\,0)$ are characterized by desorption features between 100 and 250 K. The peak around 135 K corresponds to Mg-bonded NO, whereas the broad peak near 240 K can be assigned to Ni-bonded NO [12,43]. An adsorption energy of ~15 kcal/mol can be estimated from the TPD data for NO on Ni sites of $Ni_{0.06}Mg_{0.94}O(1\,0\,0)$. An even larger NO adsorption energy is found for Cr sites of $Cr_{0.07}Mg_{0.93}O(1\,0\,0)$. The NO-TPD spectra for the $NO/Cr_{0.07}Mg_{0.93}O(1\,0\,0)$ system (top panel in Fig. 7) exhibit two well-separated desorption features at 100–160 and 250–340 K. The features around room temperature correspond to Cr-bonded NO and are associated with an adsorption energy of ~20 kcal/mol [12].

A comparison of the results in Figs. 6 and 7 points to a strong link between the electronic properties of the $TM_xMg_{1-x}O(1\,0\,0)$ systems and the NO adsorption energy. An identical result is found in DF slab calculations examining the adsorption of NO or CO (see Fig. 8) [12]. The extent of band (oxide)–orbital (adsorbate) mixing varies substantially from one dopant to another [12]. This can be explained using simple models for adsorbate bonding [12,33]. One can get an approximate expression for the bonding energy (Q) derived from the interaction between the lowest unoccupied molecular orbital (LUMO) of the adsorbate and the OS of an oxide

$$Q\alpha(\beta_{\mathrm{LUMO\text{–}OS}})^2/(E_{\mathrm{LUMO}} - E_{\mathrm{OS}}) \quad (1)$$

where $\beta_{\mathrm{LUMO\text{–}OS}}$ is the resonance integral for the interacting levels, and E_{OS} and E_{LUMO} are the energies of the oxide OS and the adsorbate LUMO, respectively. Clearly, there is a relationship between the energy position of the dopant electronic levels and the chemical reactivity of a mixed-metal oxide. This relationship is not linear, because one must also consider the number of states with low stability provided by a dopant agent [9,12]. In addition, several factors can affect the strength of a metal–NO or metal–CO bond [12,33,44,45].

Metal-doped MgO can be very efficient as a catalyst for the destruction of SO_2 [7,16,46,47]. Fig. 9

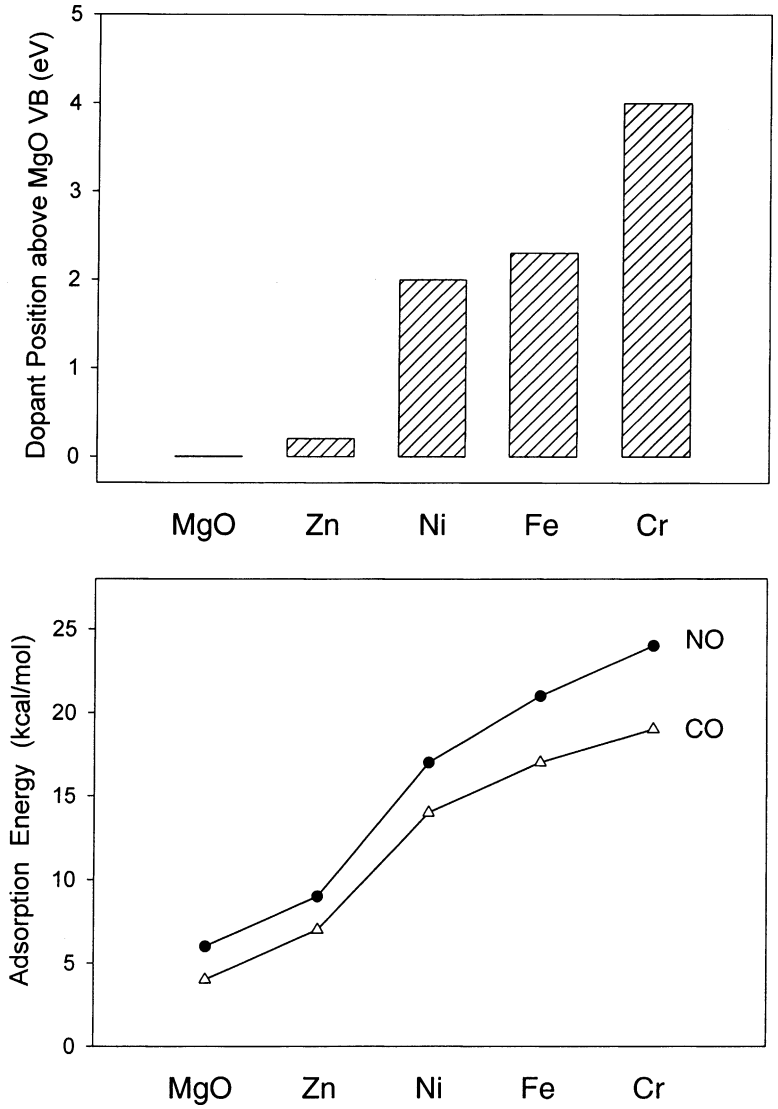

Fig. 8. Top panel: DF calculated position for the dopant levels in $TM_{0.06}Mg_{0.94}O(1\,0\,0)$ surfaces (TM = Zn, Ni, Fe, Cr). The values are reported with respect to the top of the MgO valence band. Bottom panel: calculated (DF) adsorption energies for NO (solid dots) and CO (empty triangles) on the $TM_{0.06}Mg_{0.94}O(1\,0\,0)$ surfaces (from Ref. [12]).

displays S 2p photoemission spectra recorded after adsorbing SO_2 on $TM_xMg_{1-x}O(1\,0\,0)$ surfaces at 300 K [16]. In the case of SO_2 on $Zn_{0.06}Mg_{0.94}O(1\,0\,0)$ and $Ni_{0.06}Mg_{0.94}O(1\,0\,0)$, the spectra are well fitted by a set of two doublets that indicate the formation of SO_3 and SO_4 on the mixed-metal oxides. There is no dissociation of SO_2 and the chemistry of the adsorbate is similar to that found on pure $MgO(1\,0\,0)$ [42]. DF slab calculations indicate that the Zn and Ni atoms embedded on the magnesium oxide lattice interact weakly with the LUMO of SO_2, inducing a negligible elongation of the S–O bonds [16]. A different behavior is seen on $Fe_{0.07}Mg_{0.93}O(1\,0\,0)$ and $Cr_{0.07}Mg_{0.93}O(1\,0\,0)$, where the complete dissociation of SO_2 produces features for atomic sulfur in the S 2p region [16,42]. An identical trend is found with XANES after adsorbing

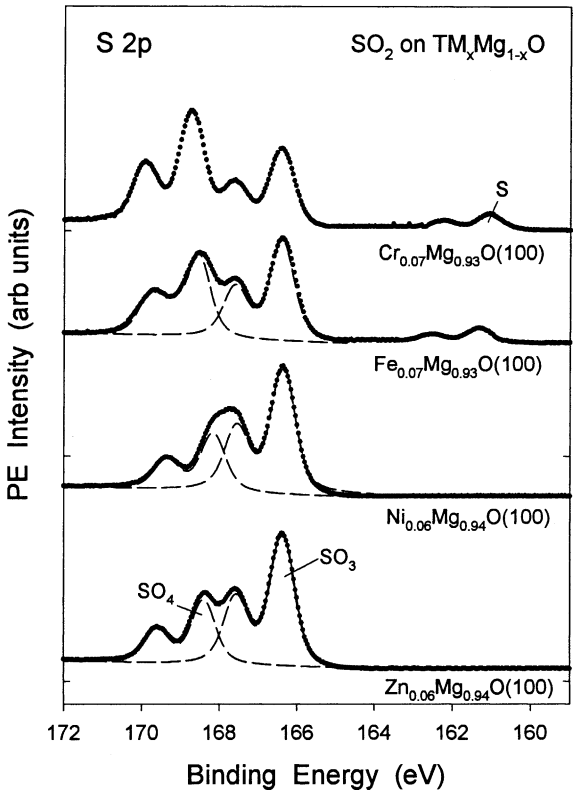

Fig. 9. S 2p spectra for the adsorption of SO_2 on $TM_xMg_{1-x}O$-(1 0 0) surfaces at 300 K (from Ref. [16]).

SO_2 on $TM_{0.06}Mg_{0.94}O(1\,0\,0)$ powder catalysts [16]. Results of photoemission, XANES and DF calculations suggest that the $Fe_xMg_{1-x}O$ and $Cr_xMg_{1-x}O$ systems should be the best catalysts for $DeSO_x$ processes [16,42]. This expectation fully agrees with the results of catalytic tests, which show $Cr_xMg_{1-x}O$ as a very efficient $DeSO_x$ catalysts and $Zn_xMg_{1-x}O$ as a very poor one [7,47]. The catalytic activity of $Fe_xMg_{1-x}O$ is not as high as that of $Cr_xMg_{1-x}O$, but this can be compensated by promoting $Fe_xMg_{1-x}O$ with alkali metals [46,47].

The cases of $Cr_xMg_{1-x}O$ and $Fe_xMg_{1-x}O$ are particularly interesting because the dopant element is "trapped" in a relatively low oxidation state. Cr_2O_3 and Fe_2O_3 (with the metal cations in a "+3" oxidation state) are the most common oxides of chromium and iron. But Cr^{2+} and Fe^{2+} can be expected from a charge balance in $TM_xMg_{1-x}O$. Indeed, results of core-level photoemission and XANES indicate that the formal oxidation state of Cr and Fe atoms in $TM_xMg_{1-x}O$ is close to "+2" [42,47]. The behavior of $Cr_xMg_{1-x}O$ and $Fe_xMg_{1-x}O$ illustrates a fundamental property for designing chemically active mixed-metal oxides: the second metal or dopant agent is not fully oxidized (i.e., not in a high oxidation state) and provides occupied electronic states with a low stability. This property makes possible effective interactions between the oxide surface and the LUMO of SO_2 [16,42], with subsequent S–O bond cleavage.

5. Electronic and chemical properties of $Ce_{1-x}Zr_xO_2$ and $Ce_{1-x}Ca_xO_2$

The studies discussed in the previous three sections show the importance of electronic effects when dealing with the activity of mixed-metal oxide catalysts. To enhance the redox properties and thermal stability of pure ceria in automobile-exhaust catalysts, zirconia is often mixed as an additive to form solid solutions of the $Ce_{1-x}Zr_xO_2$ type [17,18]. It has been suggested that ceria structural modifications mediated by zirconia [19,48] and zirconia-stabilized defects in ceria [49] are responsible for the special properties of $Ce_{1-x}Zr_xO_2$. Contributions from "electronic effects" cannot be ruled out [18].

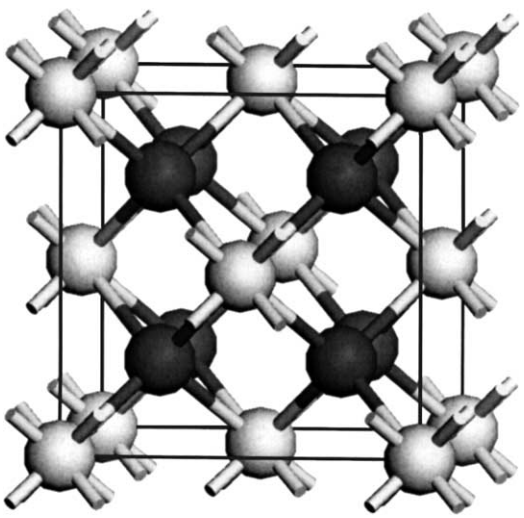

Fig. 10. Structure for pure CeO_2. The dark spheres represent O atoms.

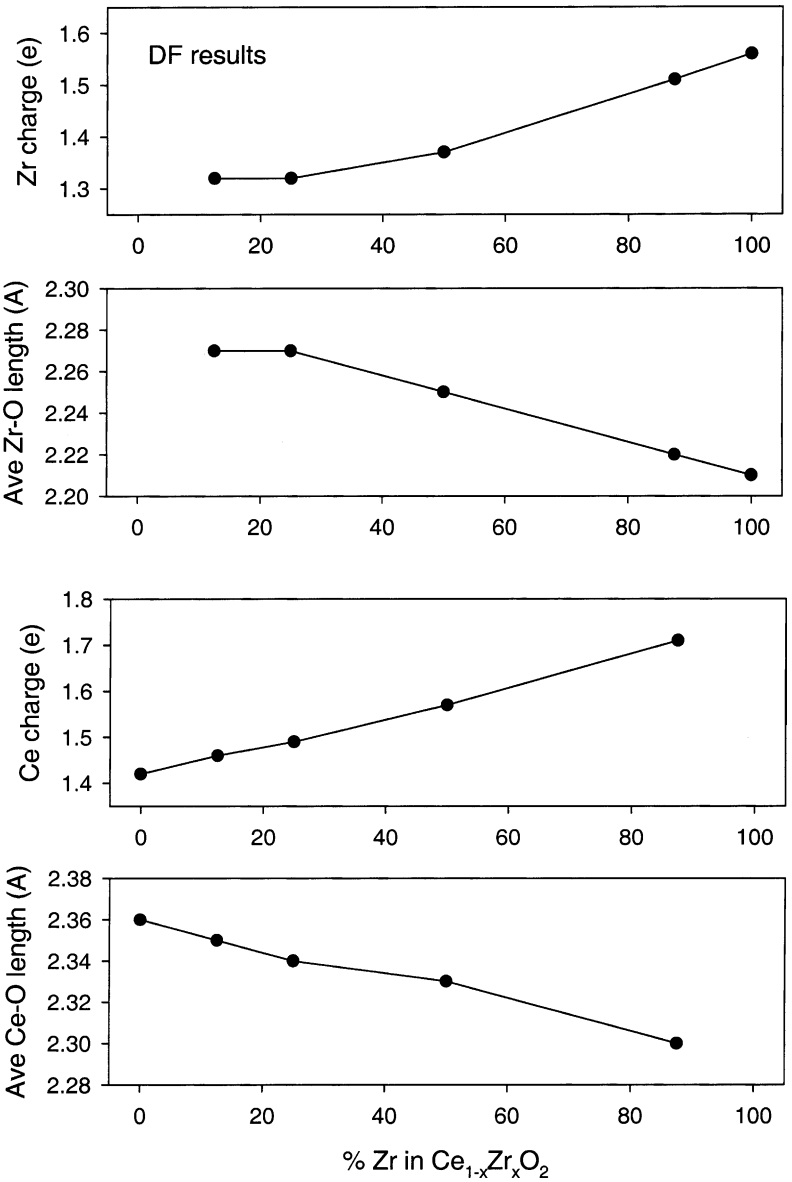

Fig. 11. DF results for bulk $Ce_{1-x}Zr_xO_2$ in a cubic structure. The two top panels show the calculated Zr charge and average Zr–O bond length. The bottom two panels display the calculated Ce charge and the average Ce–O bond length (from Ref. [18]).

Pure ceria adopts a fluorite structure (Fig. 10) [17,39]. In $Ce_{1-x}Zr_xO_2$ the cations are distributed in a fluorite-type subcell; tetragonal and cubic structures are possible [18,19,48]. Table 3 lists lattice constants calculated (DF) for bulk CeO_2 and cubic $Ce_{1-x}Zr_xO_2$ [18]. As the content of Zr increases, there is a reduction in the lattice constant of the oxide. An identical result has been found in XRD studies for several $Ce_{1-x}Zr_xO_2$ systems [48]. The lattice constant decrease is a consequence of the smaller size of Zr^{4+} (0.84 Å) with respect to Ce^{4+} (0.97 Å) [18,48]. The DF calculations indicate that this difference in size is quite important for the local structure of the metal cations [18]. Even within a cubic structure, the Zr

Table 3
DF calculated lattice constant (a) for CeO_2 and $Ce_{1-x}Zr_xO_2$

	a (Å)
CeO_2	5.46 (5.4108)[a]
$Ce_{0.875}Zr_{0.125}O_2$	5.44
$Ce_{0.75}Zr_{0.25}O_2$	5.39
$Ce_{0.5}Zr_{0.5}O_2$	5.30
$Ce_{0.25}Zr_{0.75}O_2$	5.17
$Ce_{0.125}Zr_{0.875}O_2$	5.15
ZrO_2	5.11

[a] XRD value for bulk CeO_2 [18].

atoms exhibit a structural perturbation that leads to different types of Zr–O distances and non-equivalent O atoms in the $Ce_{1-x}Zr_xO_2$ compounds. This prediction is consistent with the results of XANES measurements at the O K-edge [18,50]. In essence, it is very difficult for the Zr atoms to adopt the large metal–oxygen distances expected in a lattice of CeO_2. The perturbations in the Zr–O coordination sphere could enhance the mobility of oxygen when going from ceria to ceria–zirconia mixed oxides [18].

Several theoretical studies indicate that there is a large degree of covalency in CeO_2, ZrO_2 and $Ce_{1-x}Zr_xO_2$ [50]. In the valence bands of these oxides there is a very significant amount of metal character. Upon the addition of Zr to CeO_2, the positive charge on Zr is smaller than in pure ZrO_2, whereas the positive charge on Ce is larger than in pure CeO_2. This is illustrated in the results of Fig. 11 for bulk $Ce_{1-x}Zr_xO_2$ in a cubic structure [18]. Interestingly, when Zr replaces Ce in ceria, the Zr–O distances obtained are larger than in the corresponding ZrO_2 system, and at the same time the Ce–O distances become shorter than in the initial CeO_2 compound. The variations in cation charge seen in Fig. 11 track changes in cation–oxygen distances: the larger the metal–oxygen bond length, the smaller the positive charge on the cation (i.e. less interaction with oxygen). Thus, structural and electronic perturbations go together in the $Ce_{1-x}Zr_xO_2$ systems.

Calcium can be used as a dopant agent instead of zirconium [19,51]. Because Ca is bigger than Ce [51], the $Ce_{1-x}Ca_xO_2$ mixed-metal oxides have larger cell parameters than pure CeO_2 [52]. The doping of ceria with Ca induces an elongation in the Ce–O bond lengths that leads to a reduction in the charge of the Ce cations [52]. For example, in $Ca_{0.25}Ce_{0.75}O_2$, the positive charge on the Ce centers is ~1.32e versus 1.41e in pure CeO_2 [52]. In contrast, the charge on the Ca cations (1.84e) is bigger than in pure CaO (1.66e). These trends (the more electropositive cation becomes

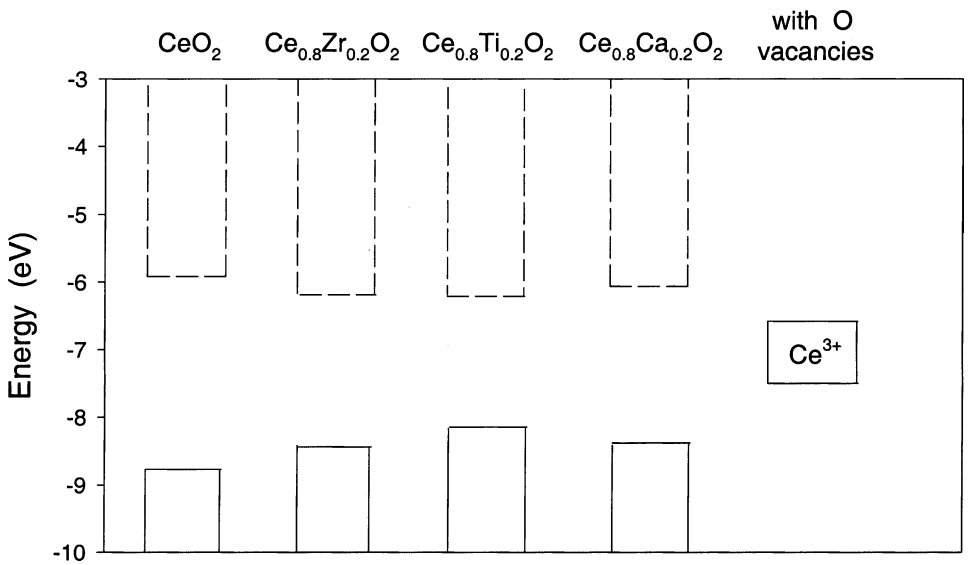

Fig. 12. Energy position for the valence and conduction bands of CeO_2, $Ce_{0.8}Zr_{0.2}O_2$, $Ce_{0.8}Ti_{0.2}O_2$ and $Ce_{0.8}Ca_{0.2}O_2$ (DF calculations). The empty and OS are indicated by dashed and solid lines, respectively. The right side of the figure shows the position for the occupied "Ce^{3+}" states when O vacancies are introduced in the oxides (from Ref. [50]).

more ionic, whereas the less electropositive undergoes an increase in its covalency) agree with the Barr model [2,25,26], but the increase in the charge of calcium is expected since it has a formal oxidation state of "+4" in stoichiometric $Ce_{1-x}Ca_xO_2$. In fact, since calcium cannot reach a "+4" oxidation state, the mixed-metal oxide may be forced to release oxygen to achieve a charge balance [51,52].

A dopant agent can enhance the chemical reactivity of a host oxide by facilitating the formation of O vacancies [5,8,29]. For example, doping of ceria with Zr, Ti or Ca induces relatively minor narrowing of the band gap (less than 1 eV), and no OS appear well above the host valence band (see Fig. 12). However, the dopants produce structural perturbations in the lattice of ceria that make easier a loss of oxygen [17–19,51], which leads to the appearance of cerium 4f OS ∼2 eV above the CeO_2 valence band (Fig. 12). These "Ce^{3+}" states are well positioned for bonding interactions with orbitals of adsorbates [9].

Fig. 13 shows N 1s and valence spectra for the adsorption of NO_2 at 300 K on a partially reduced

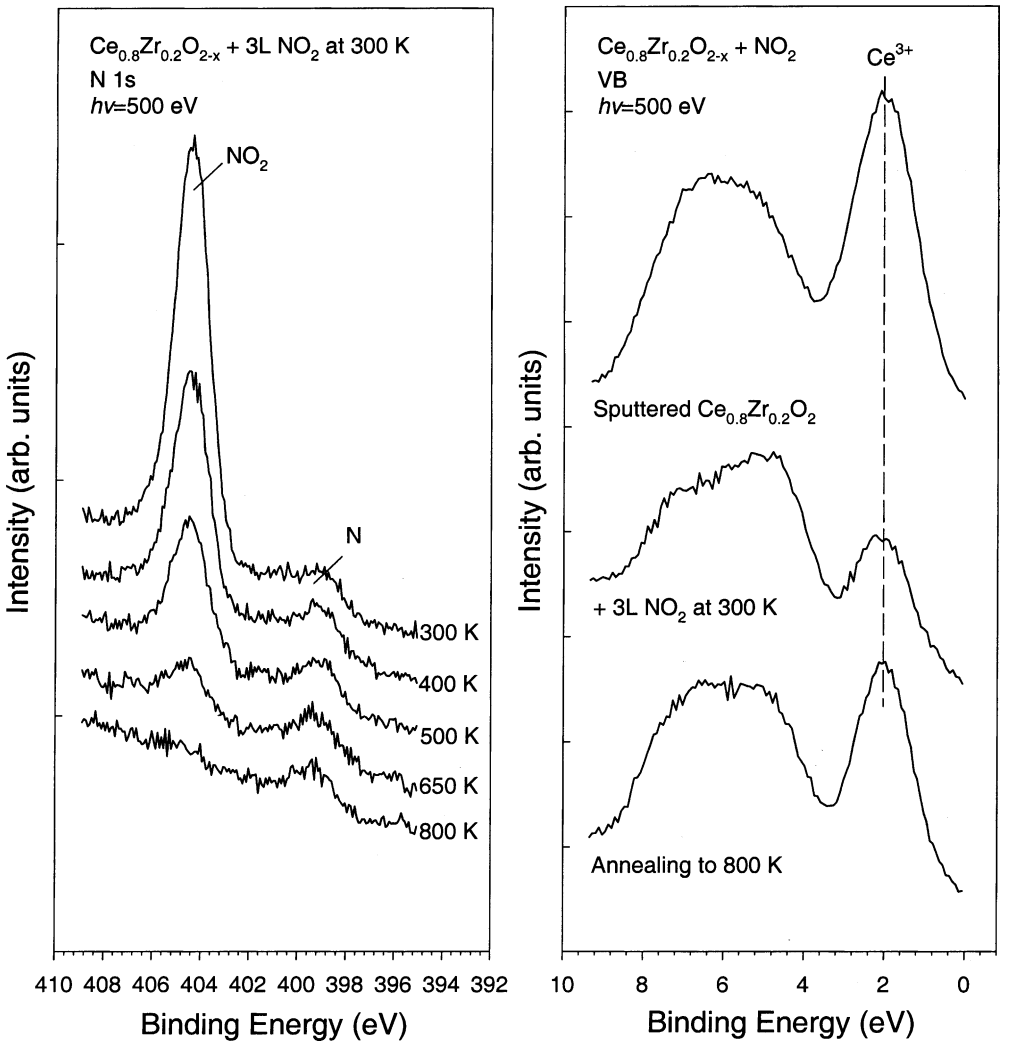

Fig. 13. N 1s spectra (left panel) and valence-band spectra (right panel) for the adsorption of NO_2 on a partially reduced $Ce_{0.8}Zr_{0.2}O_{2-x}$(1 1 1) surface. NO_2 gas was dosed at 300 K, and the surface was progressively annealed at the indicated temperatures (from Ref. [50]).

$Ce_{0.8}Zr_{0.2}O_{2-x}$(1 1 1) surface [50]. Upon dosing of the molecule there is a large drop in the intensity of the "Ce^{3+}" feature in the valence region. This feature regains intensity when the sample is annealed to 800 K for inducing the desorption of the adsorbed NO_2. From these results, it is clear that the adsorbate preferentially interacts with the "Ce^{3+}" sites of the oxide surface. An identical conclusion can be reached after examining the adsorption of NO and SO_2 on the $Ce_{0.8}Zr_{0.2}O_{2-x}$(1 1 1) surface [50,52]. Furthermore, the presence of "Ce^{3+}" centers allows the cleavage of N–O or S–O bonds.

6. Conclusions

From the studies discussed in this review, it is clear that electronic effects cannot be easily neglected when explaining the behavior or dealing with the design of mixed-metal oxide catalysts. Metal ↔ oxygen ↔ metal electronic interactions are common in mixed-metal oxides and can lead to substantial changes in the chemical properties of the cations. This is particularly true in the case of ABO_3 perovskites (A = Pb, Ca, Sr, Li, K, Na; B = Ti, Zr, Nb), and it is an important phenomenon to consider when mixing AO and BO_2 oxides for catalytic applications. The trends in the behavior of metal-doped MgO illustrate a basic principle in the design of mixed-metal oxide catalysts for $DeNO_x$ and $DeSO_x$ operations. The general idea is to find metal dopants that upon hybridization within an oxide matrix remain in a relatively low oxidation state and at the same time induce occupied electronic states located well above the valence band of the host oxide.

Acknowledgements

Over the years many people have contributed to the studies mentioned above: L.D. Andrews, S. Azad, J.L. Brito, S. Chaturvedi, J. Dvorak, J. Evans, A. Etxeberria, M. Fernández-García, D. Fischer, J. García, L. González, J.C. Hanson, J. Hrbek, A. Iglesias-Juez, T. Jirsak, J.Y. Kim, J.Z. Larese, G. Liu, A. Maiti, C.H.F. Peden, M. Pérez, D. Tyson-Smith, and L.-Q. Wang. My special thanks to all of them. I am particularly grateful to J.L. Brito and J. Evans for introducing me into the "magical world" of mixed-metal oxide catalysis and for pointing out interesting issues in this area. The research carried out at Brookhaven National Laboratory was supported by the US Department of Energy (Chemical Sciences Division, DE-AC02-98CH10886).

References

[1] C. Noguera, Physics and Chemistry at Oxide Surfaces, Cambridge University Press, Cambridge, UK, 1996.
[2] M.J. Guittet, J.P. Crocombette, M. Gautier-Soyer, Phys. Rev. B 63 (2001) 125117.
[3] F.S. Galasso, Structure, Properties and Preparation of Perovskite-type Compounds, Pergamon Press, Oxford, 1969.
[4] Proceedings of the Symposium on the Characterization of Mixed-metal Oxide Catalysts, 215th National Meeting of the American Chemical Society, Dallas, TX, American Chemical Society, Washington, DC, 1998.
[5] L.G. Tejuca, J.L.G. Fierro, J.M.D. Táscon, Adv. Catal. 36 (1989) 237.
[6] E. Heifets, R.I. Eglitis, E.A. Kotomin, J. Maier, G. Borstell, Phys. Rev. B 64 (2001) 235417.
[7] J. Evans, H. Lee, in: S.V. Rao (Ed.), Topics in Environmental Catalysis, Interscience, New York, 2001, pp. 187–214.
[8] H.H. Kung, Transition Metal Oxides: Surface Chemistry and Catalysis, Elsevier, Amsterdam, 1989.
[9] J.A. Rodriguez, Theoret. Chem. Acc. 107 (2002) 117.
[10] A. Martínez, J. Nakamura, A. Fujimori, J. Anglada, F. García-Viesca, Unpublished.
[11] J.A. Rodriguez, A. Etxeberria, L. González, A. Maiti, J. Chem. Phys. 117 (2002) 2699.
[12] J.A. Rodriguez, T. Jirsak, M. Pérez, L. González, A. Maiti, J. Chem. Phys. 114 (2001) 4186, and references therein.
[13] K. Nagaoka, T. Karasuda, K. Aika, J. Catal. 181 (1999) 160.
[14] K. Tomishige, Y. Chen, K. Fujimoto, J. Catal. 181 (1999) 91.
[15] J.A. Rodriguez, M. Pérez, T. Jirsak, L. González, A. Maiti, J.Z. Larese, J. Phys. Chem. B 105 (2001) 5497.
[16] J.A. Rodriguez, T. Jirsak, L. González, J. Evans, M. Pérez, A. Maiti, J. Chem. Phys. 115 (2001) 10914.
[17] A. Trovarelli, Catal. Rev. Sci. Eng. 38 (1996) 439.
[18] J.A. Rodriguez, J.C. Hanson, J.-Y. King, G. Liu, A. Iglesias-Juez, M. Fernández-García, J. Phys. Chem. B 107 (2003) 3535.
[19] G. Balducci, M. Islam, J. Kaspar, P. Fornasiero, M. Graziani, Chem. Mater. 12 (2000) 677.
[20] J.A. Rodriguez, J.C. Hanson, S. Chaturvedi, A. Maiti, J.L. Brito, J. Chem. Phys. 112 (2000) 935.
[21] J.A. Rodriguez, J.C. Hanson, S. Chaturvedi, A. Maiti, J.L. Brito, J. Phys. Chem. B 104 (2000) 8145.
[22] J.A. Rodriguez, J. García, L. González, Chem. Phys. Lett. 365 (2002) 380.
[23] J. Goniakowski, C. Noguera, Surf. Sci. 365 (1996) L657.
[24] B. Meyer, J. Padilla, D. Vanderbilt, Faraday Discuss. 114 (1999) 395.

[25] T.L. Barr, J. Vac. Sci. Technol. A 9 (1991) 1793.
[26] T.L. Barr, C.R. Brundle, Phys. Rev. B 46 (1992) 9199.
[27] J.A. Rodriguez, S. Azad, L.-Q. Wang, J. García, A. Etxeberria, L. González, J. Chem. Phys. 118 (2003) 6562.
[28] J.A. Rodriguez, J. García, A. Etxeberria, L. González, A. Maiti, in preparation.
[29] V.E. Henrich, P.A. Cox, The Surface Science of Metal Oxides, Cambridge University Press, Cambridge, 1994.
[30] L.-Q. Wang, K.F. Ferris, G.S. Herman, J. Vac. Sci. Technol. A 20 (2002) 239.
[31] A. Ikeda, T. Nishimura, T. Morishita, Y. Kido, Surf. Sci. 433–435 (1999) 520.
[32] D.C. Sorescu, C.N. Rusu, J.T. Yates, J. Phys. Chem. B 104 (2000) 4408.
[33] E. Shustorovich, R.C. Baetzold, Science 227 (1985) 876.
[34] J.A. Rodriguez, J.M. Ricart, A. Clotet, F. Illas, J. Chem. Phys. 115 (2001) 454.
[35] A.W. Sleight, B.L. Chamberland, Inorg. Chem. 7 (1968) 1673, and references therein.
[36] B.C. Gates, J.R. Katzer, G.C.A. Schuit, Chemistry of Catalytic Processes, McGraw-Hill, New York, 1979.
[37] J.L. Brito, A.L. Barbosa, J. Catal. 171 (1997) 467.
[38] Manuscript in press.
[39] A.F. Wells, Structural Inorganic Chemistry, 6th ed., Oxford University Press, New York, 1987.
[40] J. Miller, A.G. Sault, N.B. Jackson, L. Evans, M.M. Gonzales, Catal. Lett. 58 (1999) 147.
[41] C. Mazzochia, C. Aboumrad, C. Diagne, E. Tempesti, J.M. Hermmann, J.M. Thomas, Catal. Lett. 10 (1991) 181.
[42] J.A. Rodriguez, T. Jirsak, M. Pérez, S. Chaturvedi, M. Kuhn, L. González, A. Maiti, J. Am. Chem. Soc. 122 (2000) 12362.
[43] C. Xu, W.S. Oh, Q. Guo, D.W. Goodman, J. Vac. Sci. Technol. A 14 (1996) 1395.
[44] A. Rochefort, R. Fournier, J. Phys. Chem. 100 (1996) 13506.
[45] F. Illas, N. López, J.M. Ricart, A. Clotet, J.C. Conesa, M. Fernández-García, J. Phys. Chem. B 102 (1998) 8017.
[46] A. Pieplu, O. Saur, J.-C. Lavalley, O. Legendre, C. Nedez, Catal. Rev. Sci. Eng. 40 (1998) 409.
[47] I. Fisher, L. Zhang, Y. Wu, J. Evans, H. Lee, in preparation.
[48] G. Vlaic, R. Di Monte, P. Fornasiero, E. Fonda, J. Kašpar, M. Graziani, J. Catal. 182 (1999) 378.
[49] E. Mamontov, T. Egami, J. Phys. Chem. Sol. 61 (2000) 1345.
[50] G. Liu, J.A. Rodriguez, J. Hrbek, J. Dvorak, C.H.F. Peden, J. Phys. Chem. B 105 (2001) 7762.
[51] S. de Carolis, J.L. Pascual, L.G.M. Petterson, M. Baudin, M. Wójcik, K. Hermansson, A.E.C. Palmqvist, M. Muhammed, J. Phys. Chem. B 103 (1999) 7627.
[52] J.A. Rodriguez, X. Wang, J.C. Hanson, G. Liu, A. Iglesias-Juez, M. Fernandez-Garcia, J. Chem. Phys. 119 (2003) in press.